



# Evolution of carbon nanotubes and their metallurgical reactions in Al-based composites in response to laser irradiation during selective laser melting

Nesma T. Aboulkhair<sup>a,\*</sup>, Marco Simonelli<sup>a</sup>, Ehab Salama<sup>b</sup>, Graham A. Rance<sup>c</sup>, Nigel C. Neate<sup>c</sup>, Christopher J. Tuck<sup>a</sup>, Amal M.K. Esawi<sup>b</sup>, Richard J.M. Hague<sup>a</sup>

<sup>a</sup> Centre for Additive Manufacturing (CfAM), Faculty of Engineering, University of Nottingham, Nottingham, NG8 1BB, UK

<sup>b</sup> Department of Mechanical Engineering, The American University in Cairo (AUC), AUC Avenue, P.O. Box 74, New Cairo, 11835, Egypt

<sup>c</sup> Nanoscale and Microscale Research Centre, University of Nottingham, Nottingham, NG7 2RD, UK

## ARTICLE INFO

### Keywords:

Selective laser melting  
Aluminium  
Multi-walled carbon nanotubes MWCNT  
Microstructure  
Indentation testing

## ABSTRACT

Aluminium-based composites reinforced with carbon nanotubes are widely sought for their outstanding metallurgical and structural properties that largely depend on the manufacturing route. In this work, the process-structure-property relationship for a composite made from high-energy-ball-milled pure Al and multi-walled carbon nanotubes (MWCNT) processed by laser powder-bed-fusion additive manufacturing was investigated. The response of MWCNT to laser irradiation and their interfacial reactions with Al were probed in a holistic investigation. X-ray diffraction confirmed the partial transformation of C into Al-carbides in addition to the presence of some nano-crystalline graphitic materials. Microscopy revealed evidence of carbides segregation at the melt pool boundaries as well as migration along the build direction. Micro Raman spectroscopy showed that laser irradiation promoted re-graphitisation in MWCNT, reducing the amount of defects introduced by milling. Two types of  $Al_4C_3$  formed as a result of the metallurgical reaction between Al and MWCNT. These were needle-like and hexagonal  $Al_4C_3$  and their mechanisms of formation, direct precipitation and dissolution-precipitation, respectively, were explained in light of the thermal profile experienced by the material during melting and solidification. Large scale electron backscatter diffraction showed that there is no distinctive texture developing during melting and solidification. Micro- and nano-indentation testing showed uniform mechanical properties.

## 1. Introduction

Pure aluminium has the lowest strength compared to its alloys, which is why Al is mostly used in the form of an alloy [1] despite the success of studies on strengthening pure Al [2–5]. Al alloys have attractive properties, such as low density ( $2.7 \text{ gm/cm}^3$ ), high strength [1], adequate hardenability [6], good corrosion resistance [7–9], and excellent weldability [6]. As the demand for technologically complex and economically sustainable products increases, opportunities for Al within industry are expected to further increase. Al is suitable for numerous applications, such as automobiles [10], food and beverage packaging, building construction, electricity transmission, transportation infrastructure, defence, aerospace, and machinery and tools production [7,9]. One of the methods to strengthen pure Al is mechanical alloying with a reinforcing material, such as multi-walled carbon nanotubes (MWCNT), which adds strength through their characteristic architecture that grants them their superior mechanical properties [11].

The powder-bed fusion technology selective laser melting (SLM) is

now being used for *in-situ* production of metal matrix composites (MMC) [12] as well as amorphous/glassy (metallic glass), nanocrystalline, or ultrafine-grained structures [13]. Gu et al. used SLM's *in-situ* alloying capability to produce novel AlSi10Mg-based [14], Al-TiC [15], and AlSi10Mg-TiC [16] composites with multiple reinforcements leading to enhanced mechanical properties. All these attempts focussed on reinforcing Al alloys with various types of carbides. Wang et al. [17] added carbon nanotubes (CNT) to AlSi10Mg via ball milling with the aim of material strengthening. Although the SLM material showed higher tensile strength with CNT, the reason behind this was unclear since the phases present after SLM were not precisely identified. Zhao et al. [18] reported the presence of only  $\alpha$ -Al and eutectic Si in the same composite based on X-ray diffraction patterns, suggesting that the CNT have decomposed during processing. Du et al. [19] used a simple wet mixing method to attach CNT to the surface of AlSi10Mg particles. The mixing technique was unable to disperse the CNT into the matrix homogeneously, as clusters of CNT were present. The authors reported grain refinement to be promoted by the presence of CNT during

\* Corresponding author.

E-mail address: [nesma.aboulkhair@nottingham.ac.uk](mailto:nesma.aboulkhair@nottingham.ac.uk) (N.T. Aboulkhair).

processing, improving the material's hardness. However, the tensile properties deteriorated with CNT, a finding that contradicts Wang et al. [17]. Similar outcomes were observed when adding CNT to IN625 using a similar methodology, but post-process heat treatment improved the tensile strength significantly [20]. Du et al. [19] have demonstrated that the fracture surfaces contained CNT clusters to which the failure was attributed via crack-bridging. Therefore, SLM of a CNT-MMC might not necessarily lead to their full decomposition.

Selective laser melting fabricates complex structures from loose powder, adopting a layer-based additive manufacturing approach [21]. Unmatched degrees of design freedom and part complexity are among its promises. Furthermore, the process imposes rapid cooling and solidification rates during processing, which produces parts with characteristically fine microstructures that grant the fabricated parts superior performance. Although SLM commonly uses readily available commercial alloys, the development of new, specifically-tailored powder mixtures is of growing interest. A promising route to produce bespoke SLM feedstock is blending metal powders with diverse properties [22]. Coating a material of high reflectivity with another of high laser absorptivity could also be a means for better material processability.

The studies in the literature in this field of *in-situ* alloying of Al-alloys focus on the AlSi10Mg alloy, which is already processable by SLM. Investigating the effect of MWCNT on the processability of the difficult-to-process pure Al is yet to be explored. An Al-MWCNT composite is made up of a material that has low absorptivity (Al), which already poses challenges to SLM processing and another which has extremely high absorptivity (CNT > 99%). To the authors' knowledge, the response of this particular composite to laser irradiation in SLM has not been previously investigated. Therefore, the aim of this paper is to investigate the possibility of processing Al-MWCNT as a composite material, using and exploiting the high heat and cooling rates in SLM, studying the type and architecture of reinforcements produced, thereby providing a new route for the processing of novel material combinations.

## 2. Experimental work

### 2.1. High energy ball milling of Al-MWCNT composite

Elicarb® MWCNT synthesized by chemical vapour deposition were acquired from Thomas Swan Corporation (UK) with 10–12 nm diameter and lengths extending to tens of microns (Fig. 1 (a)). The 200-mesh size pure aluminium (Al) was supplied by ALPOCO (Fig. 1 (b)). Al powder was high-energy ball-milled (HE-BM) with 2 wt% MWCNT in stainless

steel vials in a Retsch planetary ball mill PM400 MA with a ball-to-powder weight ratio of (5:1) for 1 h at 400 RPM. The choice of MWCNT content and ball milling parameters was educated from earlier studies [11,23–25]. Minute amounts, 0.18  $\mu\text{L}$  per vial, of high purity Ethyl alcohol were added to the milling vials to balance the repetitive powder cold welding and fracturing to achieve uniform dispersion of MWCNT. All powder handling took place in a glove box under controlled argon atmosphere. The morphology of the mechanically-alloyed powder was imaged using a Hitachi TM3030 scanning electron microscope (SEM) with a 15 kV accelerating voltage using a backscatter electron detector and a JOEL 7100F FEG-SEM (Field Emission Gun – Scanning Electron Microscope) whereas its flowability was tested using a Hall flowmeter funnel following the ASTM standard B213 [26]. The powder was dried overnight at 70 °C because this can reduce porosity by 50% [27] since gas phases in the starting powder, such as hydrogen due to surface moisture, significantly suppress densification [28].

### 2.2. In-situ alloying of Al-MWCNT composite by selective laser melting

The powder was sieved (75- $\mu\text{m}$ ) then processed using a Realizer GmbH SLM-50® (Germany) machine, equipped with a 100 W Yttrium fibre laser (YLM-100-AC) with a 20  $\mu\text{m}$  spot size, under inert atmosphere (Ar) with an oxygen level below 0.2%. Single walls (5 mm high), *i.e.* individual tracks accumulating along the build direction, were constructed onto a polished Al substrate using a 100 W laser power, 40  $\mu\text{m}$  layer thickness, and 250 mm/s scan speed. The platform on which the samples were built was maintained at 200 °C. Further, 5 × 5 × 5 mm<sup>3</sup> test cubes were fabricated using a hatch spacing of 50  $\mu\text{m}$  and a pre-melt scan strategy. The idea behind the pre-melt scan strategy is to promote particles sintering prior to laser irradiation with the full power [29] and act as an *in-situ* drying step thus reducing gas porosity [27]. In order to assess the effect of MWCNT addition on the processability of pure Al, Al powder without MWCNT was ball milled using the same milling parameters to experience a similar amount of severe plastic deformation. The unreinforced powder was also processed by SLM following the same procedure for the reinforced material.

### 2.3. Selectively laser melted Al-MWCNT samples metallurgical properties characterisation

Three sets of cubes were cross-sectioned, polished, etched, and microscopically imaged. One set was etched using Keller's reagent (etchant 1) by swabbing (2–3 swabs), the second was subjected to deep etching by immersion in Keller's reagent for 5 min, and the third was

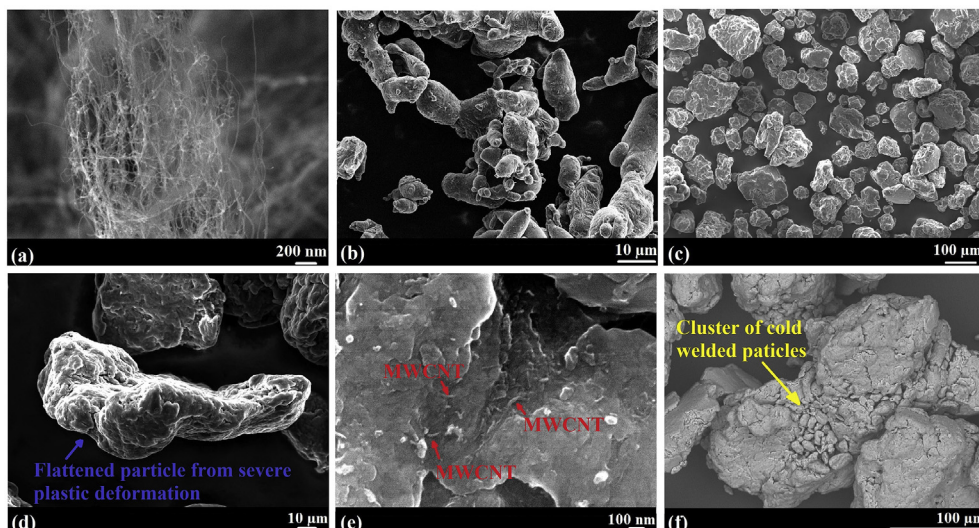


**Fig. 1.** SEM images showing the morphology of (a) multi-walled carbon nanotubes, (b) pure Al powder, (c) high energy ball-milled Al-MWCNT powder demonstrating the irregular morphology, and (d) some particles that were flattened by severe plastic deformation. MWCNT embedded inside the Al particles is presented in (e) and (f) shows a significantly large particle that contains much finer cold-welded particles.

immersed in 25 ml methanol, 25 ml hydrochloric acid, 25 ml nitric acid, and 1 drop of hydrofluoric acid (etchant 2) for 20–30 s. A Nikon Eclipse LV100ND optical microscope and a JOEL 7100F FEG-SEM were used to study the microstructure of the etched samples. A Hilton Brooks PW1050 X-ray diffractometer using Cu K $\alpha$  radiation at a wavelength of 0.154 nm operating at 40 kV and 20 mA was used to collect the XRD patterns for the powder and bulk samples. The speed of the scan was set to 1° per minute and the step size was 0.05. A thin lamella was prepared using focussed ion beam milling (FIB) on a FEI Quanta 200 3D Dual Beam FIB-SEM for transmission electron microscopy (TEM) investigation. A JOEL-2000FX TEM and a JOEL-2100+ TEM with W and LaB<sub>6</sub> filament electron guns, respectively, were used to study the reinforcements. Micro Raman spectroscopy was performed using a Horiba Jobin Yvon LabRAM HR Raman spectrometer. Spectra were acquired using a 532 nm laser at 0.34 mW power, a 100x objective lens, and a 300  $\mu$ m confocal pinhole. For each powder sample, single point measurements from five random areas were acquired over the range 100–4000  $\text{cm}^{-1}$ . A lateral spectroscopic map of the cross-sectioned sample was obtained over the range 150–1800  $\text{cm}^{-1}$  in 1  $\mu$ m steps. The spatial resolution was  $\sim 1 \times 1 \times 5 \mu\text{m}$  (xyz). Electron backscatter diffraction (EBSD) maps were collected using a JOEL 7100F FEG-SEM equipped with Oxford Instruments AZtec HKL Advanced EBSD System (with NordlysMax3) for crystallographic characterisation. Maps were collected at an accelerating voltage of 15 kV.

#### 2.4. Selectively laser melted Al-MWCNT samples mechanical properties characterisation

A Buehler Vickers hardness tester was used to measure the microhardness on the polished samples, applying 10 indentations per sample at a load of 3 N. The samples were also nanoindentation hardness tested using a MTS XP nano-indenter. A Berkovich diamond tip was used applying 25 indentations per sample, taking into account the indenter tip area function, as well as thermal drift correction. Tests were performed in accordance with the ASTM standard E2546 [30] in a load-controlled mode. The maximum indentation load was set to 500 mN and the spacing between adjacent indentations was set to 100  $\mu$ m.

### 3. Results & discussion

#### 3.1. Mechanically-alloyed MWCNT reinforced aluminium powder characterisation

Upon irradiating the powders with a laser beam, there exists an energy balance between conductivity (K) and absorptivity (A). The absorptivity or reflectivity of the powder depends not only on the physiochemical properties of the powder but also on their granular morphology and apparent density. The properties of the powder being one of the process variables [31] that highly affect processing [32]. In contrast to irregular particles, spherical particles mean better flowability [33] and higher packing density; two characteristic features that are pre-requisites in SLM [13,34]. The challenge here is that mechanical alloying produces powder that has been subjected to severe plastic deformation, resulting in particles' fracturing and cold welding [3,5]. Therefore, it had an irregular morphology (Fig. 1 (c), (d) and (f)), compromising the flowability. The flowability of the composite was 90 s/50 g; this is relatively poor compared to other alloys processed by SLM [29,35]. However, this can be overcome through deploying the pre-melt scan strategy during SLM processing [35].

#### 3.2. Selective laser melting of pure Al and Al-MWCNT composite

Olakanmi [36] studied the effect of SLM parameters on processing pure Al. Fully consolidated samples were not achieved, as the powder seemed to sinter rather than melt due to its high reflectivity. In the current study, it was possible to fabricate single walls from pure Al.

However, their structural integrity was very poor, suggesting limited processability, in agreement with [36], contrary to the intact Al-CNT walls. All attempts to fabricate cubic samples from pure Al failed as instead of forming cubes, the material created lumps. Therefore, it can be asserted that MWCNT addition significantly improved the processability where cubic samples were successfully fabricated.

Zhao et al. [18] asserted that the laser energy needed to process AlSi10Mg coated with MWCNT was higher than that needed for the uncoated powder, suggesting that the laser energy absorbed by the MWCNT was not efficiently transferred to the AlSi10Mg particles. In the current study, the fact that the same amount of energy that was unable to process pure Al was capable of processing the Al-MWCNT powder is an indication that the good physical interaction and bonding between the MWCNT and Al particles through Van der Waal's forces, realised by severe plastic deformation, assisted the energy transfer. The difference between the current study and that of [18], besides the use of pure Al instead of AlSi10Mg, is the mixing process. Zhao et al. [18] used slurry ball milling, which allowed the dispersion of the MWCNT into the powder without subjecting them to severe plastic deformation, i.e. the morphology of the powder was not largely deformed as in the case of ball milling, although the contact between MWCNT and Al particles was compromised. However, balling milling embeds the MWCNT inside the Al particles rather than just coating Al with MWCNT [24], as can be seen in Fig. 1 (e). The type of bonding between the Al matrix and the MWCNT reinforcement when using high energy ball milling is a mechanical bond realised by mechanical alloying [37].

#### 3.3. Characterisation of the selectively laser melted Al-CNT composite

Both types of porosity – gas and lack of fusion [27,29] – formed in the SLM samples (see Fig. 2). The lack of fusion pores have irregular morphologies besides being larger in size [29] and they sometimes take the half-moon shape characteristic of the melt pools. They also occasionally contained un-melted powder. Some pores had high aspect ratios with their lengths spanning across several layers, where the length of one pore was nearly 450  $\mu$ m, whereas the layer thickness was 40  $\mu$ m.

The microstructure of the sample (Fig. 2) exhibited regions that were rich in Al and others that were decorated with secondary phases that were confirmed to be Al-carbides, as will be demonstrated later. In order to reveal the Al<sub>4</sub>C<sub>3</sub> phase under the optical microscope, etchant number (2) was used where all the chemical elements were diluted in water. According to Zhou et al. [38], deep etching in water-containing reagents leads to the formation of Al(OH)<sub>3</sub> and the liberation of CH<sub>4</sub> according to the chemical reaction (Al<sub>4</sub>C<sub>3</sub> + 12H<sub>2</sub>O → 4Al(OH)<sub>3</sub> + 3CH<sub>4</sub>), leaving expanded impressions on the sample where the Al<sub>4</sub>C<sub>3</sub> initially was. This aided in visualising the distribution of the carbides along the length of the sample. As per Fig. 2 (e), a relatively higher density of the carbides can be seen closer to the top layer (the darker phase). The source of these carbides is the MWCNT present in the material where the Al reacts with C according to the chemical reaction (4Al + 3C → Al<sub>4</sub>C<sub>3</sub>) under the inert atmosphere (Ar) used in the SLM process, as will be explained later, along with the mechanism of their formation. Therefore, it is not unexpected to see these form in close proximity to the MWCNT, indicating that migration of the MWCNT and the carbides with additional layers potentially occurred due to the thermal gradient in the material. The Al<sub>4</sub>C<sub>3</sub> phase decorated the matrix mostly by segregating along the boundaries/overlap of the scan tracks (Fig. 2 (f)) and, unlike other Al alloys processed by SLM, it was not possible to observe the individual melt pools across the sample. However, the shell-shaped melt pools were observed in the cross-section of the top layer, suggesting that the repetitive melting and solidification due to the penetration of the laser energy into the preceding layers is wiping away this structure along the depth of the sample.

The XRD patterns for the powder and bulk samples are shown in Fig. 3 (a). The MWCNT, as-received and milled pure Al powder patterns were collected as reference materials. The patterns demonstrate the

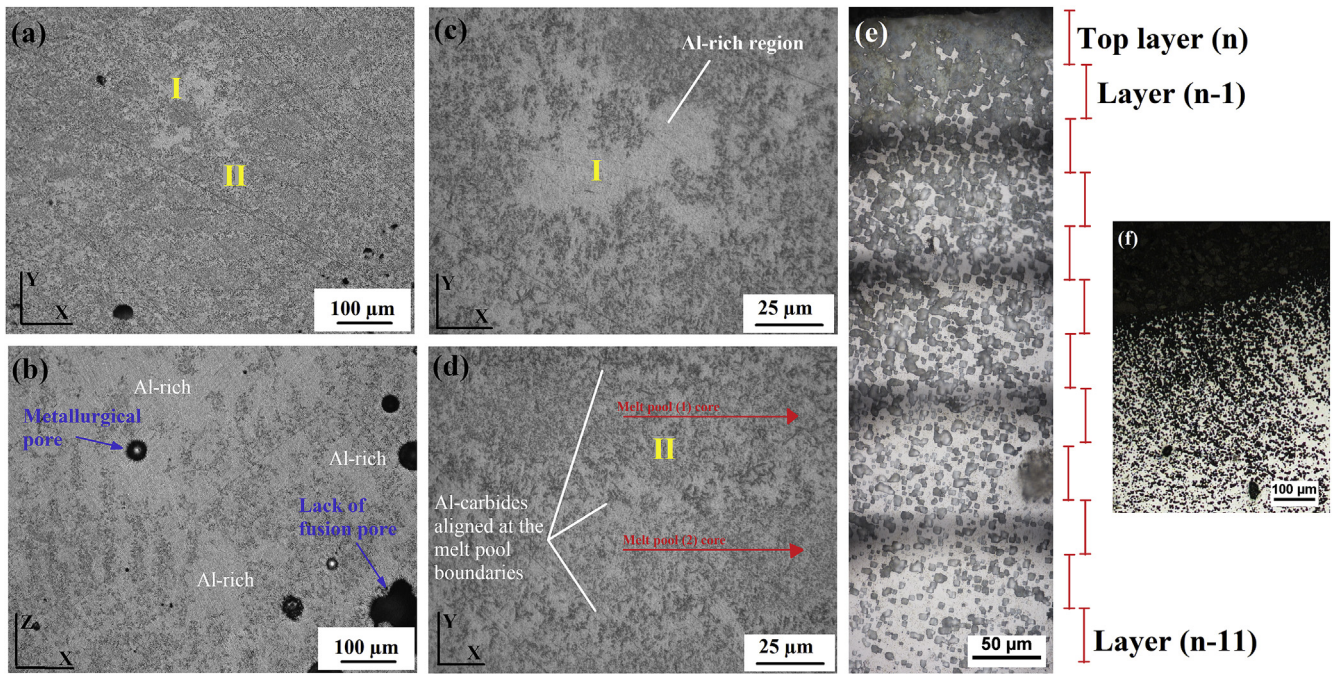


**Fig. 2.** Microstructure of the material showing the distinction between the Al-rich (I) and Al-carbides-rich (II) regions (a-d). The distribution of the carbides along the melt pool boundaries on a cross-sectional view of the XY plane of the sample and their migration to the top of the sample with layer addition on the XZ plane are presented in the stitched image in (e) and image (f).

crystal structure refinement after ball milling in the form of peaks broadening and shortening [3]. The pattern returned from the Al-2wt% MWCNT powder sample shows the four characteristic peaks for Al corresponding to the (111), (200), (220), and (311) planes in the face-centred cubic (FCC) crystal structure. No peaks for MWCNT or aluminium carbides were observed, agreeing with earlier published results [39]. Potential reasons are the low concentration of MWCNT, strain effects, or damaging the MWCNT during milling, which can yield them amorphous. The last factor can be excluded as the XRD scan from the SLM sample revealed the presence of a MWCNT peak at  $26.6^\circ$  (in the same position as the peak observed when scanning MWCNT on their own but significantly weaker and narrower) alongside some aluminium carbide peaks reflecting the formation of  $Al_4C_3$ . MWCNT surviving laser irradiation during AM processing has been reported when using laser deposition techniques despite the introduction of a higher density of defects [40]. Heterogeneous nucleation of carbides is connected to the presence of defects in MWCNT where C atoms are at a higher energy state [41], e.g. the dangling carbon atoms at the nanotube termini or dislocations within the CNT sidewalls [38]. The high surface tension of Al (860 mN/m at  $750^\circ\text{C}$ ) creates poor wetting between the molten Al and the MWCNT with a high contact angle ( $\sim 130\text{--}140^\circ$  [42]). The high surface tension forces the MWCNT to move closer to each other leading to the potential formation of clusters. Hence favouring stir casting as a conventional processing technique to help disperse the MWCNT into the Al matrix. However, after  $Al_4C_3$  starts to form, the contact angle decreases by nearly 70% to roughly  $50\text{--}70^\circ$ . The improved wetting promotes infiltration of the metal into the MWCNT allowing better dispersion [40] and enhances the interfacial properties [42]. The measurements for the amounts of the various phases, calculated by the relative intensity ratio method which is a semi-quantitative method, were as expected for an Al-2wt% MWCNT composite. Carbon/graphite,  $Al_4C_3$ , and pure Al accounted for 1.4%, 0.9%, and 97.8%, respectively.

The lattice parameter was calculated using Bragg's law from the diffraction patterns to be 0.40 nm, agreeing with the standard for pure Al, as per the ICDD PDF 00-004-0787. The full width at half maximum height (FWHM) for each of the characteristic peaks was measured from the collected patterns of the as-received Al powder, the high energy ball

milled Al-MWCNT powder, and the SLM Al-MWCNT sample. These are presented in Fig. 3(b). High-energy ball milling resulted in the most significant peak broadening due to the severe plastic deformation experienced by the material and the introduction of large amounts of strain. This is in agreement with similar studies in the literature [2]. The peaks in the SLM sample were narrower than those of the ball milled powder but broader than those of the as-received Al powder. During SLM, the powder melts and solidifies, which in the course of the process can cause relative coarsening as the material is maintained at higher temperatures, i.e. in a molten state, for longer. The elevated temperatures at which SLM operates can also promote dislocation annihilation, reducing the density of dislocations. This reverses the influence of severe plastic deformation on the dislocation's density during ball milling. A change in peak intensities was also observed; the intensity of the (111) peak was reduced whereas the (200) peak showed a higher intensity. This can potentially be explained as having a preferred orientation of the Al crystals in the SLM sample. This will be further explained in the EBSD section later on.

The Al matrix decorated with  $Al_4C_3$  can be seen in the TEM image in Fig. 4 (a) with the respective selected area diffraction patterns (SADP) in Fig. 4(g and h). The carbides mostly segregated along the boundaries of the Al grains (Fig. 4(a and b)), showing a lower content towards the cores. Their sizes ranged from tens to hundreds of nanometers. The carbides solidified with either a needle-like or well-crystallised hexagonal morphology, as shown in Fig. 4 (d) and (e). This further supports the XRD results; a fraction of the MWCNT reacted with the Al during melting and solidification to form aluminium carbides due to the elevated processing temperatures involved in SLM. This reaction is favoured at a temperature corresponding to the operation temperature of the cell ( $\sim 970^\circ\text{C}$  [43]). According to Ci et al. [42], Al starts to react with CNT under a protective atmosphere of argon in the range of temperatures between  $450$  and  $950^\circ\text{C}$  and with the chemical reaction that produces  $Al_4C_3$  occurring at temperatures above the melt point of aluminium ( $650^\circ\text{C}$ ). It is believed that the high melt pool temperatures associated with the process, therefore, promoted this reaction, hence the high content of carbides formed. As per Novak et al. [43], the needle-like  $Al_4C_3$  crystals form directly by precipitation from C

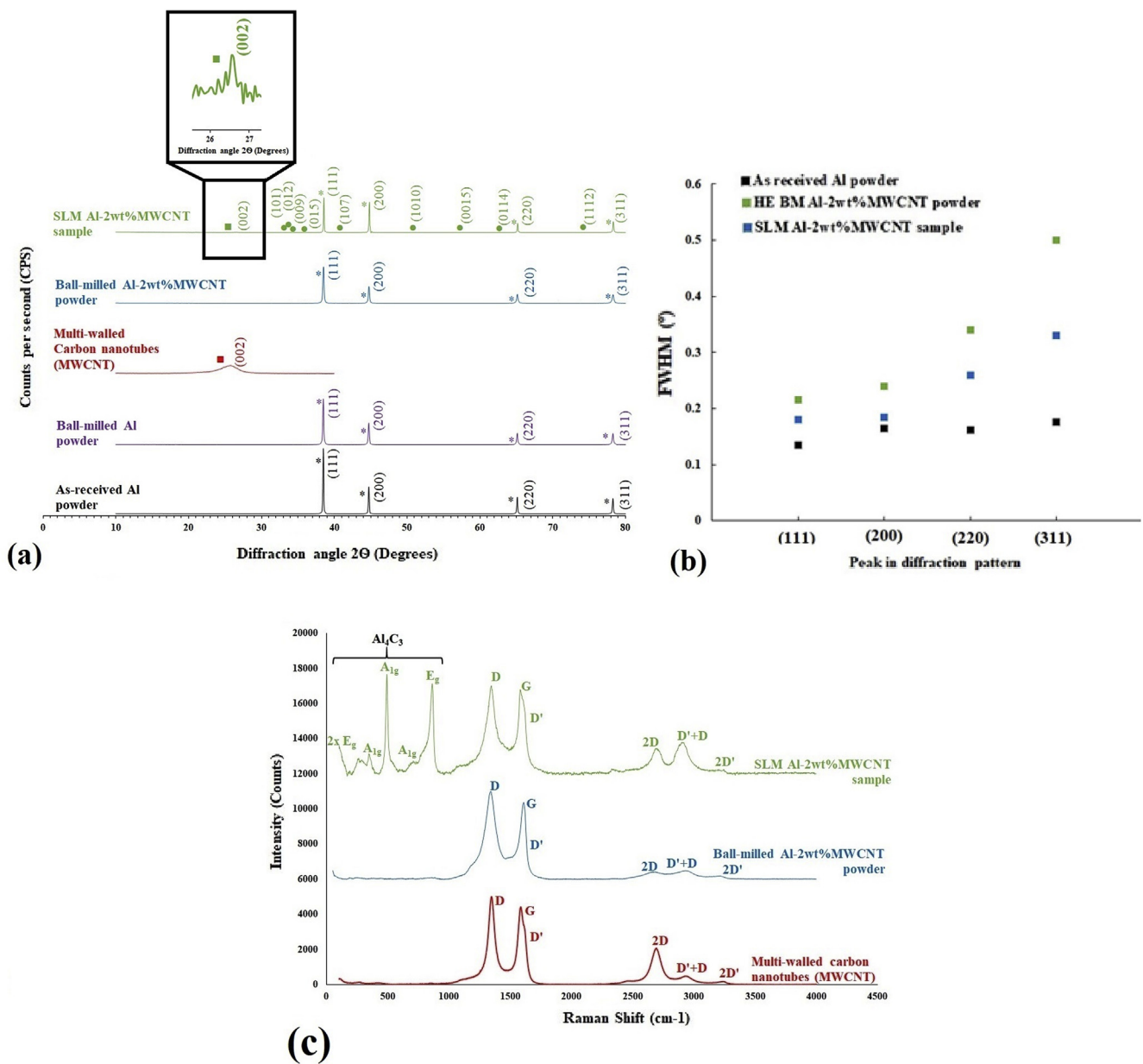


**Fig. 3.** The XRD patterns for the raw materials, ball-milled powders, and SLM samples are shown in (a) with the inset showing a zoomed-in view for the MWCNT peak in the SLM sample. The peaks for Al are denoted by stars (\*), the peaks for MWCNT are denoted by squares (■), and those for Al<sub>4</sub>C<sub>3</sub> are denoted by circles (●). (b) A comparison between the FWHM of the peaks of as-received Al powder, high energy ball milled HE-BM Al-2wt%MWCNT powder, and SLM Al-2wt%MWCNT. Raman spectra collected from the MWCNT, the Al-2wt%MWCNT powder, and the SLM sample are presented in (c).

dissolving in the molten Al that is supersaturated with C during cooling. On the other hand, the hexagonal particles form by a dissolution-precipitation mechanism [44]. Upon attaining supersaturation whilst the molten Al is in contact with the C source, MWCNT in this study, Al<sub>4</sub>C<sub>3</sub> crystals expand laterally into hexagons; the hexagonal face corresponding to the basal plane of the Al<sub>4</sub>C<sub>3</sub>, with the c-axis of the hexagon being preferentially oriented parallel to that of the substrate. These hexagonal features then act as barriers hindering growth in the vertical direction so lateral expansion is favoured. The growth direction can be clearly seen in Fig. 4 (b) and (e). They also act as protective layers reducing further consumption of the MWCNT.

Despite the transformation of some of the MWCNT upon laser irradiation into needle-like crystals and hexagonal particles of Al<sub>4</sub>C<sub>3</sub>, MWCNT that survived the laser irradiation can be seen in Fig. 5. A more effective and reliable way to observe the MWCNT was deep etching in Keller's reagent, a process in which the Al<sub>4</sub>C<sub>3</sub> decomposes through the

reaction with water in the etchant [38,43] and the MWCNT are preferentially revealed [39], as shown in Fig. 5 (a) and (b). It is worth noting that the rates of decomposition for the two different types of carbides with deep etching vary, hence the hexagonal particles were still partly visible on the sample surface when the needle-like ones had already decomposed. Another example for MWCNT within one of the needle-like Al<sub>4</sub>C<sub>3</sub> is presented in Fig. 5 (c), where a necking connection between a needle-like and a hexagonal crystal of Al<sub>4</sub>C<sub>3</sub> is clearly observed.

The high cooling rates imposed during the process resulted in a high density of dislocations, forming dislocation networks, loops, and forests that can be seen in Fig. 6 (a) and (b). The introduction of high densities of dislocation in SLM parts has been reported for a range of materials [45] and a correlation between the process parameters used and the density of dislocations created has been established by Ma et al. [46]. The more reheating and re-melting in the process, the lower the density

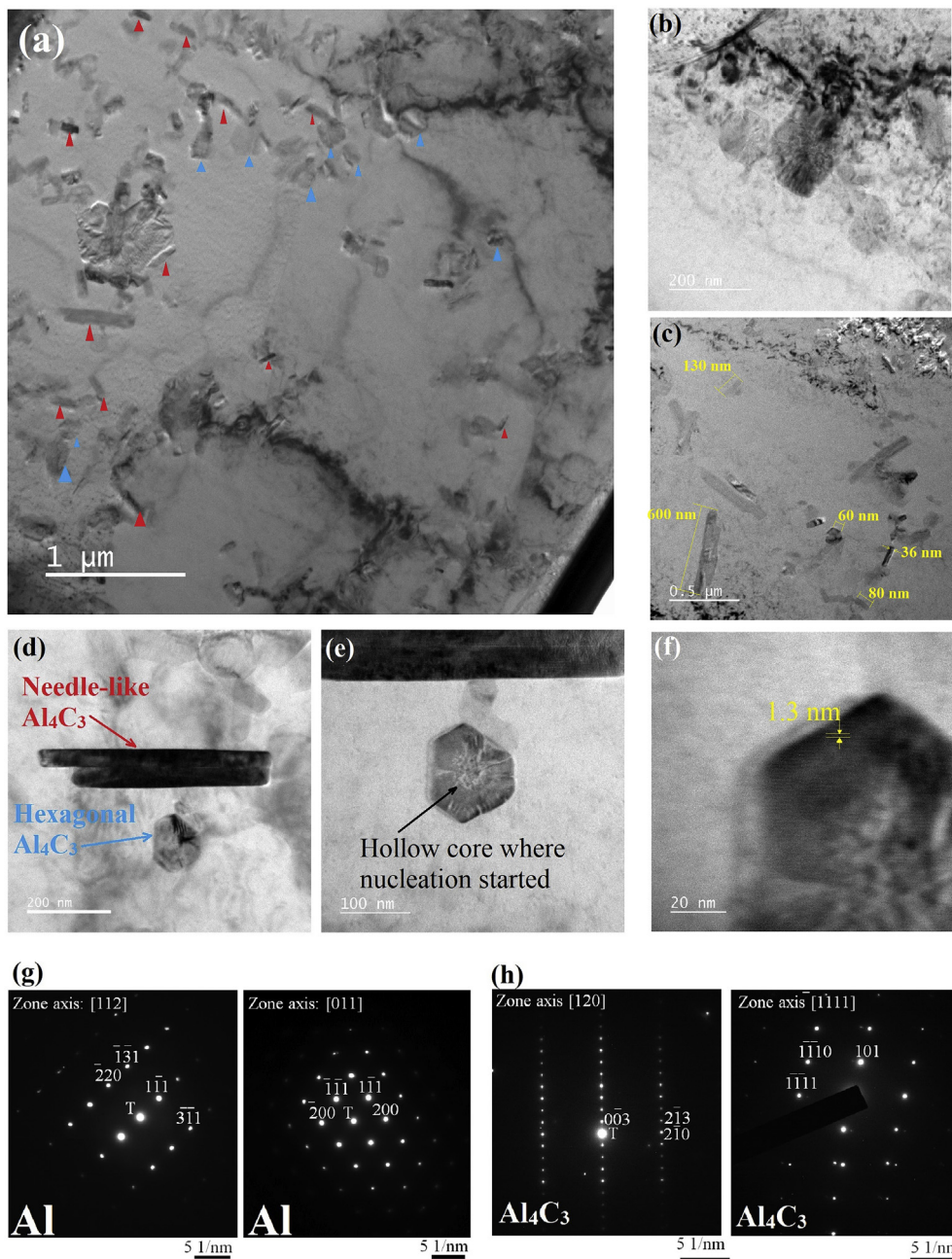


Fig. 4. (a) TEM images showing the two types of aluminium carbides in the Al-2wt% MWCNT SLM samples with their range of sizes in (b) and classification in (d). The hollow core of the hexagonal carbide nucleated is shown in (e) with the layered spacing in (f). The SADP for Al and Al<sub>4</sub>C<sub>3</sub> are provided in (g) and (h).

of dislocations due to dislocations recovery. The double-tilt capability on the TEM's sample holder was used to achieve a 90° rotation in total to reveal the side view of the carbides. This is shown in Fig. 6 (e) and (f) for the needle-like and hexagonal particles, respectively. The morphology of the needles remained the same with rotation whereas that of the hexagons changed to confirm they are hexagonal plates.

The Raman spectrum of MWCNT (Fig. 3) is consistent with that expected for graphitic nanocarbons and contains a number of diagnostic bands: (1) the G (graphite) band – an in-plane carbon-carbon stretching vibration of E<sub>2g</sub> symmetry, present in all graphitic nanostructures – at ~1590 cm<sup>-1</sup>; (2) the D (defect) band – a breathing mode of six-atom rings of A<sub>1g</sub> symmetry, requiring a defect for its activation – at ~1350 cm<sup>-1</sup>; and (3) the 2D-band (occasionally referred to as the G' band) at ~2700 cm<sup>-1</sup> [47]. The Raman spectrum of more defective nanocarbons, such as MWCNT produced by the chemical vapour

deposition method, including those used in this study, are additionally characterised by a D' band – a vibration of E<sub>2g</sub> symmetry specifically associated with disordered graphitic surface layers – at ~1620 cm<sup>-1</sup>, resulting in the asymmetric line shape of the G band and the existence of overtones (2D') and combination modes (D + D') in the higher frequency region.

The spectrum from the Al-MWCNT powder sample showed an increase in the intensity of the D band and reduction in the 2D band (both relative to the G band) indicating a decrease in the intra- and inter-layer ordering of the graphitic lattice, respectively, after milling, i.e. milling damaged the graphitic structure of the MWCNT, consistent with the results from XRD analysis where no ordered graphitic phase was observed. There is also a shift in the position of the G band to higher energy after milling, which could indicate possible charge transfer between MWCNT and Al or result from stress/strain of the graphitic

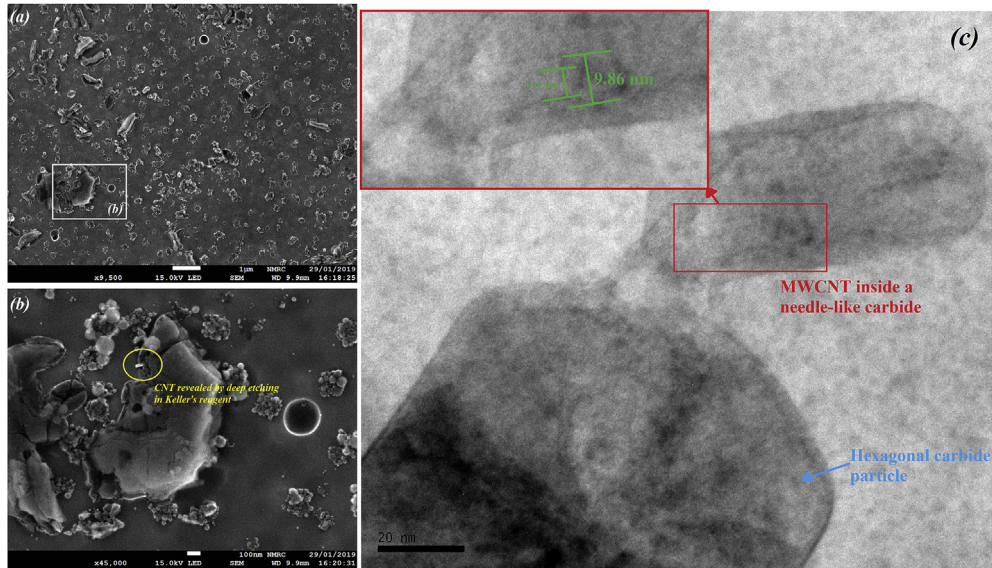


Fig. 5. Deep etching in Keller's reagent revealed the impressions of where the Al-carbides were in (a). One of the MWCNT poking out from a hexagonal  $Al_4C_3$  particle is shown in (b). MWCNT within a needle-like carbide can be seen in (c).

lattice upon binding to Al, but is most likely associated with an increase in the intensity of the D' band, symptomised by increase in the intensity of the associated combination and overtone modes and causing an apparent symmetrisation and blue shift of the band at  $\sim 1590\text{ cm}^{-1}$ .

After SLM processing, there is an apparent increase in the intensity of the 2D band and subtle reduction in the intensity of the D band (relative to the G band), accompanied by a shift in the position of the G band to approximately that observed in the parent MWCNT. This suggests that the heat generated during SLM is sufficient to induce re-graphitisation – a process expected to happen above  $1600^\circ\text{C}$  – thus increasing the intra- and interlayer structural ordering relative to the ball milled sample and justifying the observation of peaks associated with MWCNT in the XRD pattern for the SLM sample. It is important to

note that the observed band at  $\sim 2910\text{ cm}^{-1}$  is not exclusively associated with the D + D' band and contains a contribution from the C-H stretching vibrations of an aliphatic hydrocarbon impurity on the surface of the sample. This can be attributed to the PCA used during milling. False colour images (Fig. 7) derived from Raman spectroscopic mapping describe the distribution of  $Al_4C_3$  and nanocrystalline graphitic carbon (most likely associated with MWCNT) within a  $50 \times 50\ \mu\text{m}$  area of the polished cross-section of the SLM material. MWCNT – diagnosed by the intensity (as height) of the D band ( $1000\text{--}1475\text{ cm}^{-1}$ ) – are found in the majority of locations within the appraised area, indicating effective dispersion of MWCNT within the matrix, with some evidence of clustering into  $\sim 5\text{--}10\ \mu\text{m}$  aggregates.  $Al_4C_3$  – characterised by the  $A_{1g}$  vibrational mode ( $435\text{--}530\text{ cm}^{-1}$ ) – was found to be

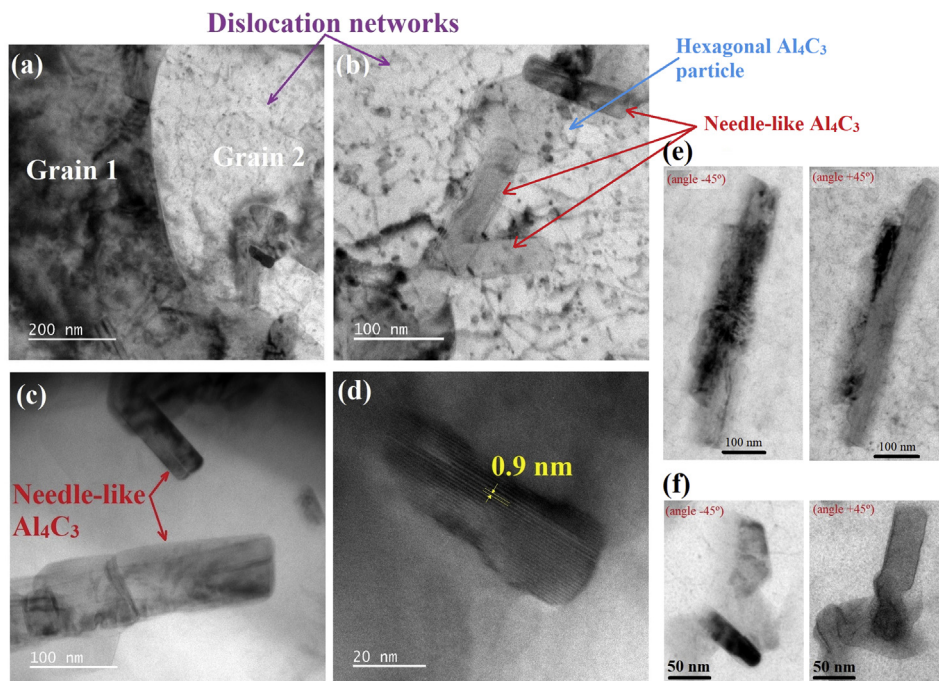


Fig. 6. High dislocation density forming networks and forest around the Al-carbides, as observed by TEM in (a) and (b). Needle-like  $Al_4C_3$  in the Al matrix is shown in (c) and the lattice fringes are in (d). Needle-like and hexagonal Al-carbides imaged using tilts of  $(-45^\circ)$  and  $(+45^\circ)$  are presented in (e) and (f).

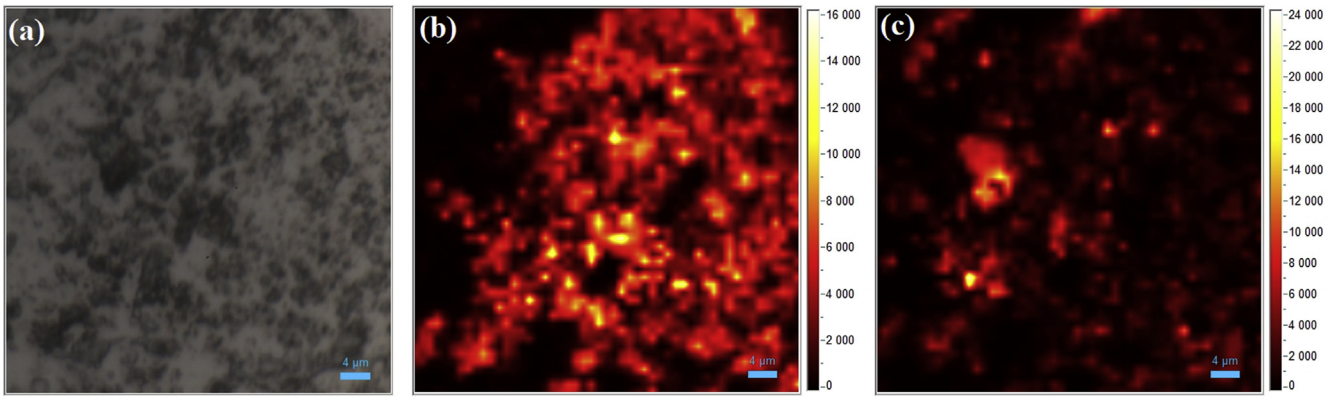


Fig. 7. Mapping using Raman spectroscopy for the area shown in the optical micrograph in (a). The maps show the distribution of (b)  $Al_4C_3$  and (c) MWCNT.

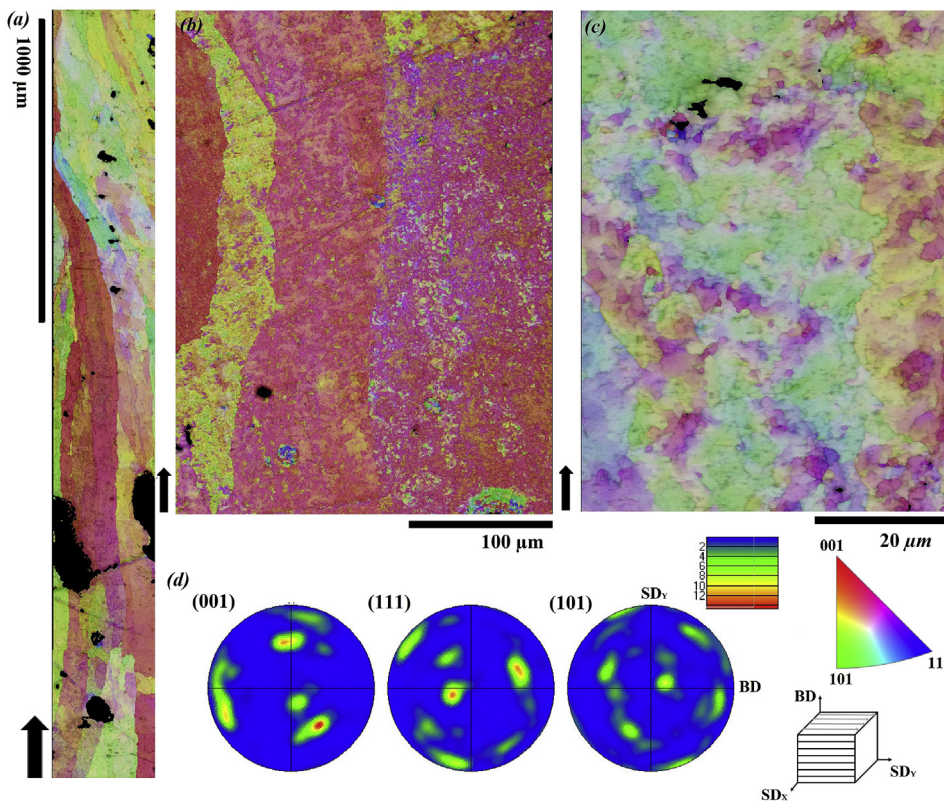


Fig. 8. (a) Inverse Pole Figure (IPF) map ( $2.86\ \mu m$  step size) showing the columnar microstructure and weak texture in the SLM samples, (b) IPF map ( $0.34\ \mu m$  step size) focussing on the columnar microstructure growing parallel to the build direction, (c) higher resolution IPF map ( $0.1\ \mu m$  step size) showing the cellular solidification within the material's columnar grains, and (d) contour pole figures showing the texture intensity in the samples. All the IPF are plotted along the build direction indicated by black arrows in the micrographs.

homogeneously distributed, yet the peaks are quite broad and ill-defined, indicating low crystallinity (Fig. 7).

The EBSD analysis showed that the grain structure has a predominant columnar morphology, as indicated in Fig. 8(a and b), which depicts the typical microstructure found in the sample with grains predominantly aligned parallel to the build direction. The grain size is however heterogeneous with grain refining as the sample height increased, *i.e.* adding more layers during processing. This implies that as layers are progressively added, the deposited structure coarsens, being sustained by heat transfer through the layers, *i.e.* material re-melting and reheating, and the epitaxial growth. Indeed the lack of constitutional undercooling (as there are no alloying elements), combined with the material's high thermal conductivity and high solidification speed intrinsic to SLM produce shallow melt pools, with heat mainly dissipated vertically, giving rise to a distinctive columnar morphology.

Large scale EBSD mapping revealed an overall weak texture with columnar grains adopting no preferential solidification direction (Fig. 8 (d) – contour pole figures). The lack of crystallographic texture is

consistently reported with the additive manufacturing literature of Al alloys: the intrinsic high conductivity of the materials implies that the “easy” growth direction (100) typical of cubic materials does not dominate the solidification of Al alloys.

As expected, given the high cooling rates typical of SLM, the sub-structure that make up the columnar grains consists of fine cellular grains, as shown in Fig. 8 (c). Energy dispersive X-ray diffraction (EDX) analysis revealed that the cell boundaries are richer in C relative to the cores. This is evidenced in the EDX map in Fig. 9. This corroborates well with the TEM investigations presented in this manuscript that indicate higher concentration of  $Al_4C_3$  at the grain boundaries. According to these findings, it can be articulated that upon reaching the operational temperature of the cells, molten Al would first react with C at the nucleation sites on the MWCNT to form  $Al_4C_3$ , then the Al starts to infiltrate through the MWCNT in the latter stage of the solidification and pushes the  $Al_4C_3$  towards the grain boundaries.

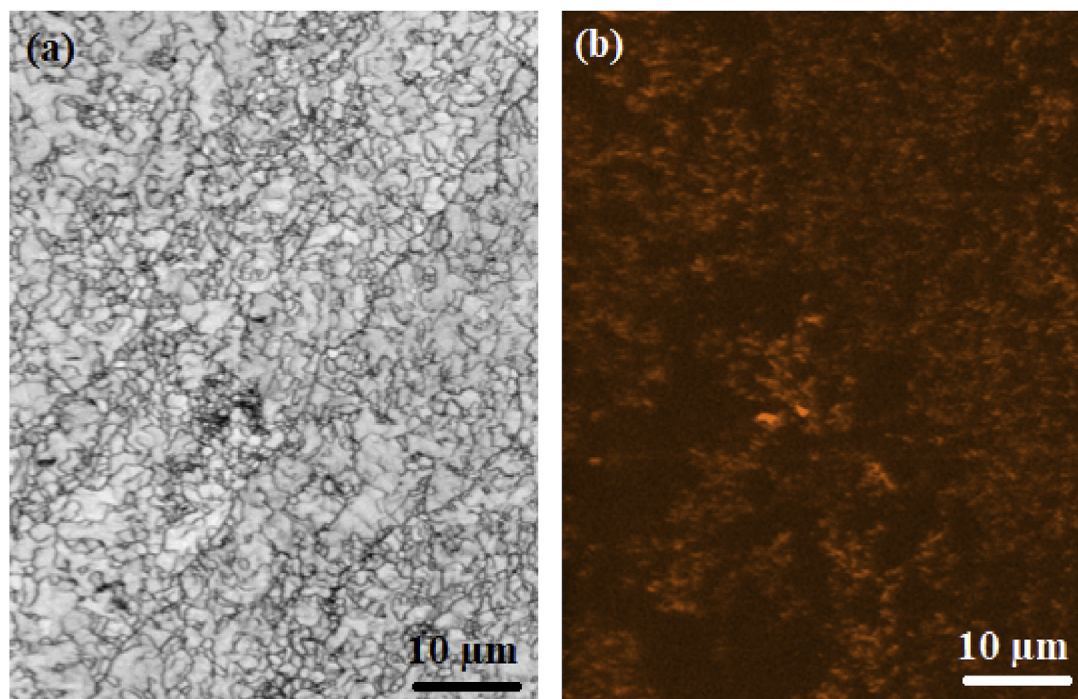


Fig. 9. Band Contrast image (a) and the corresponding EDX map for carbon (b) showing that the cell boundaries are richer in C than the cell cores.

### 3.4. The mechanical properties

The values for some of the Al-CNT composites produced by a range of conventional processes are presented in Table 1. The micro-hardness of the SLM samples collected from the plane perpendicular to the build direction (XY-plane) was  $47.0 \pm 0.4$  HV. As evident in Table 1, the material's hardness depends primarily on the fabrication method, which dictates the resultant microstructure and type of reinforcement(s). For instance, using ball milling yields materials of relatively elevated hardness owing to the grain refinement and increased density of dislocations imposed by severe plastic deformation. Mechanical mixing, spark plasma sintering, and hot isostatic pressing, on the other hand, produce a softer material. Nevertheless, variations in mechanical response exist while using the same manufacturing method. This can be attributed to differences in the types of MWCNT used, as well as the degree of dispersion realised using various mixing and milling conditions. The presence of MWCNT in the material during melting and solidification strengthens it, compared to the unreinforced equivalent, through them acting as nucleating sites as they increase the work hardening and thermal conductivity in addition to being second phases.

**Table 1**

A list of some of the hardness data reported in the literature for Al-2wt%CNT composites produced using a range of techniques.

Processing technique	Micro-hardness (HV)	Nano-hardness (GPa)	Source
Selective laser melting	$47.0 \pm 0.4$	$0.54 \pm 0.01$	This work
Cold Pressing and Sintering	50	–	[50]
Ball milling and powder metallurgy	–	0.8–1.6	[51]
	71	0.74	[52]
	137	1.24	[39]
Mechanical mixing and powder metallurgy	73	–	[40]
	74	–	[40]
Spark plasma sintering SPS	88	–	[53]
Spark plasma sintering	52	–	[53]
SPS + Hot extrusion	–	0.77	[54]
Hot Isostatic Pressing	62	–	[53]
Stir casting	69	–	[55]

The rapid melting and solidification common in SLM can be favoured to limit the reactions between MWCNT and the matrix because the reactivity increases when the matrix is in a liquid form. This requires further investigations on the effect of altering the process parameters on the extent of reactions between the Al and MWCNT. Considering the micro-hardness results, the SLM material showed results that are comparable to the cold-pressed and sintered counterpart whilst being softer than other conventional production routes. Furthermore, its nano-hardness was significantly lower (by ~55–64%) than the reference material – produced by powder metallurgy. One of the reasons behind this reduction in mechanical performance can be the partial decomposition of MWCNT when irradiated by laser in SLM forming hexagonal and needle-like  $Al_4C_3$ , as observed in the SEM and TEM images, which is not the case when processing by conventional methods. Although  $Al_4C_3$  do strengthen pure Al due to their crystallographic structure and acting as obstacles to dislocation motion, therefore hardening the material, their effect here was not as significant since they are compared to CNT reinforcements which are known to provide significantly higher hardness. In addition, the microstructure coarsening by SLM, as evidenced by the FWHM measurements from the XRD patterns analysis, contributes to softening the material. One of the mechanisms by which CNT improves a material's hardness is through refining the grain structure [48], which was compromised here by the effect of laser processing. Porosity in SLM samples is known to depress the mechanical performance of the parts manufactured. The samples prepared in this study had a relative density of  $99.52 \pm 0.02\%$ . It has also been established in the literature for CNT composites that the hardness is directly proportional to the relative density of the samples [49]. Further investigations are currently underway to optimise the SLM process parameters in order to achieve a balance between minimising the amount of porosity and defects forming in the sample and limiting the reaction between Al and MWCNT forming the  $Al_4C_3$  phase.

The indentation modulus of the SLM samples was  $64.7 \pm 0.9$  GPa, which is comparable to that of the reference material (71.5 GPa [39]), only 9% lower. This is because the modulus of a material is an intrinsic property that is controlled by the atomic bonding within. Therefore, this was not affected by the manufacturing process used to fabricate the test specimens. The hardness, on the other hand, is an engineering

property, which is influenced by the microstructure and defects in the material, among other factors. Hence, the variation in hardness with the manufacturing process.

#### 4. Summary and conclusions

An Al-MWCNT composite fabricated by high energy ball milling followed by laser powder-bed fusion was investigated. Adding MWCNT to pure Al and utilising the *in-situ* alloying capability of SLM enabled its processing for the first time, compared to the unalloyed material. The strong bond and good dispersion in the matrix promoted the energy transfer from the MWCNT to Al whilst maintaining the heat at the irradiated spot for longer, improving the melt efficiency of the material. The uniformity of MWCNT dispersion in MMC is critical to the structural capability of the material, which depends largely on the manufacturing technique, with ball milling resulting in moderate to good dispersion. The layer-by-layer additive manufacturing approach in SLM strongly influenced the reinforcement's dispersion through migration, promoting segregation at the upper layers. This phenomenon has been observed in the case of stir casting and to the authors' knowledge, it was not previously investigated in the case of SLM.

Ball milling increased the extent of disorder within and between the graphitic lattices of MWCNT and introduced small, but measurable, amounts of amorphous carbon. SLM resulted in the formation of semi-crystalline  $Al_4C_3$  and the partial re-graphitisation of MWCNT. Spectroscopic mapping indicated that (i) the carbide phase was distributed uniformly across the mapped area and (ii) clustering of MWCNT was observed, but MWCNT were present in nearly all areas within the map in lower amounts. Therefore, it can be asserted, based on the experimental evidence in this paper, that the MWCNT can survive the laser irradiation during SLM. The interfacial reactions between the MWCNT and Al resulted in an Al matrix decorated with needle-like  $Al_4C_3$ , hexagonal particles of  $Al_4C_3$ , and MWCNT. The carbides formed via two different mechanisms, namely direct precipitation and dissolution-precipitation. Dislocations forests and networks developed in the material due to the rapid melting and solidification associated with the process. The sample exhibited an overall weak texture. In some regions, columnar grains grew parallel to the build direction and in others; these were slightly inclined. These columnar grains were made up of sub-grains or ultrafine grains/cells of a random texture. A finer microstructure was observed at the top layers, which was attributed to MWCNT migration with layer addition. Despite their positive influence on the material's processability, MWCNT did not seem to grant the material superior mechanical properties as it would in the case of conventional processing.

The novel work presented in this study has led to a number of new research questions that remain to be answered. These include tailoring the ball milling conditions (including the MWCNT type and content) to control the fracturing and cold welding of the powder particles to reduce the impact of severe plastic deformation on the morphology of the powder to fulfil the SLM material requirements. Nevertheless, new approaches to powder feedstock preparations are to be devised. Further on, the SLM process parameters require optimisation to improve the relative density of the parts manufactured from the mechanically alloyed composite that can then be used in future research to monitor the effect of changing the process parameters on the material's microstructure. The response of the material produced using the route proposed in this study to heat treatments may yield rich and exciting results, considering both the microstructural transformation and the mechanical properties that are yet to be explored. It is also crucially important to investigate the macro-scale static and dynamic mechanical properties of the optimised parts produced utilising the integrated outputs from these studies.

#### Data availability

The processed data required to reproduce these findings are available to download from <https://data.mendeley.com/datasets/nxxn2fdp7t/draft?a=cab3de1c-d3e7-46bb-b3e4-da36571c114c>.

#### Acknowledgements

The authors of this work would like to acknowledge the support provided by the members of staff at the nano- and micro-scale research centre (nmRC) at the University of Nottingham, where most of the materials characterisation was conducted. Thanks to Dr Christopher Parmenter for his help with the Focussed-Ion Beam milling and Dr Michael Fay for his support with the Transmission Electron Microscopy. Dr Nesma T. Aboulkhair acknowledges the funding provided by the University of Nottingham's Anne McLaren Fellowship. Professor Amal Esawi acknowledges the financial support by the American University in Cairo.

#### Appendix A. Supplementary data

Supplementary data to this article can be found online at <https://doi.org/10.1016/j.msea.2019.138307>.

#### References

- [1] M. Tisza, *Physical Metallurgy for Engineers*, ASM International and Freund Publishing House Ltd, 2002.
- [2] N.T. Aboulkhair, Strength and Ductility of Bulk Nanostructured Aluminum Processed by Mechanical Milling, Department of Mechanical Engineering, The American University in Cairo, AUC DAR Repository, 2012.
- [3] N.T. Aboulkhair, A.M.K. Esawi, Effect of milling time and annealing on the mechanical response of mechanically milled aluminium, *Adv Mater Res-Switz* 445 (2012) 815–820.
- [4] H.J. Choi, S.W. Lee, J.S. Park, D.H. Bae, Tensile behavior of bulk nanocrystalline aluminum synthesized by hot extrusion of ball-milled powders, *Scr. Mater.* 59 (10) (2008) 1123–1126.
- [5] A.M.K. Esawi, N.T. Aboulkhair, Bi-modally structured pure aluminum for enhanced strength and ductility, *Mater. Des.* 83 (2015) 493–498.
- [6] Y. Li, D. Gu, Parametric analysis of thermal behavior during selective laser melting additive manufacturing of aluminum alloy powder, *Mater. Des.* 63 (0) (2014) 856–867.
- [7] G.E. Totten, D.S. Mackenzie, *Handbook of Aluminum: Physical Metallurgy and Processes*, 1 ed., CRC press, New York, 2003.
- [8] I.J. Polmear, *Light Alloys: Metallurgy of the Light Metals*, third ed. ed.
- [9] W.H. Hosford, *Physical Metallurgy*, second ed., CRC Press, United States of America, 2010.
- [10] H. Zhao, D.R. White, T. DebRoy, Current issues and problems in laser welding of automotive aluminium alloys, *Int. Mater. Rev.* 44 (6) (1999) 238–266.
- [11] A.M.K. Esawi, K. Morsi, A. Sayed, M. Taher, S. Lanka, Effect of carbon nanotube (CNT) content on the mechanical properties of CNT-reinforced aluminium composites, *Compos. Sci. Technol.* 70 (16) (2010) 2237–2241.
- [12] F. Chang, D. Gu, D. Dai, P. Yuan, Selective laser melting of in-situ  $Al_4SiC_4 + SiC$  hybrid reinforced Al matrix composites: influence of starting SiC particle size, *Surf. Coat. Technol.* 272 (0) (2015) 15–24.
- [13] K.G. Prashanth, H. Shakur Shahabi, H. Attar, V.C. Srivastava, N. Ellendt, V. Uhlenwinkel, J. Eckert, S. Scudino, Production of high strength Al85Nd8Ni5Co2 alloy by selective laser melting, *Additive Manufacturing* 6 (0) (2015) 1–5.
- [14] D. Gu, F. Chang, D. Dai, Selective laser melting additive manufacturing of novel aluminum based composites with multiple reinforcing phases, *J. Manuf. Sci. Eng.* 137 (2015) 0210101-11.
- [15] D. Gu, Z. Wang, Y. Shen, Q. Li, Y. Li, In-situ TiC particle reinforced Ti–Al matrix composites: powder preparation by mechanical alloying and Selective Laser Melting behavior, *Appl. Surf. Sci.* 255 (22) (2009) 9230–9240.
- [16] D.D. Gu, H.Q. Wang, D.H. Dai, P.P. Yuan, W. Meiners, R. Poprawe, Rapid fabrication of Al-based bulk-form nanocomposites with novel reinforcement and enhanced performance by selective laser melting, *Scr. Mater.* 96 (0) (2015) 25–28.
- [17] L. Wang, T. Chen, S. Wang, Microstructural characteristics and mechanical properties of carbon nanotube reinforced AlSi10Mg composites fabricated by selective laser melting, *Optik - Int. J. Light Electron. Opt.* 143 (Supplement C) (2017) 173–179.
- [18] X. Zhao, B. Song, W. Fan, Y. Zhang, Y. Shi, Selective laser melting of carbon/AlSi10Mg composites: microstructure, mechanical and electrical properties, *J. Alloy. Comp.* 665 (2016) 271–281.
- [19] Z. Du, M.J. Tan, J.F. Guo, J. Wei, Aluminium-carbon nanotubes composites produced from friction stir processing and selective laser melting, *Mater. Werkst.* 47 (5–6) (2016) 539–548.
- [20] P. Wang, B. Zhang, C.C. Tan, S. Raghavan, Y.-F. Lim, C.-N. Sun, J. Wei, D. Chi,

- Microstructural characteristics and mechanical properties of carbon nanotube reinforced Inconel 625 parts fabricated by selective laser melting, *Mater. Des.* 112 (2016) 290–299.
- [21] I. Gibson, D.W. Rosen, B. Stucker, *Additive Manufacturing Technologies*, Springer, 2010.
- [22] M. Simonelli, N.T. Aboulkhair, P. Cohen, J.W. Murray, A.T. Clare, C. Tuck, R.J.M. Hague, A comparison of Ti-6Al-4V in-situ alloying in Selective Laser Melting using simply-mixed and satellited powder blend feedstocks, *Mater. Char.* 143 (2018) 118–126.
- [23] A.M.K. Esawi, K. Morsi, A. Sayed, M. Taher, S. Lanka, The influence of carbon nanotube (CNT) morphology and diameter on the processing and properties of CNT-reinforced aluminium composites, *Compos. Appl. Sci. Manuf.* 42 (3) (2011) 234–243.
- [24] A. Esawi, K. Morsi, Dispersion of carbon nanotubes (CNTs) in aluminum powder, *Compos. Appl. Sci. Manuf.* 38 (2) (2007) 646–650.
- [25] Ehab I. Salama, Sherry S. Morad, Amal M.K. Esawi, Fabrication and mechanical properties of aluminum-carbon nanotube functionally-graded cylinders, *Materialia* 7 (2019) 100351.
- [26] Standard Test Methods for Flow Rate of Metal Powders Using the Hall Flowmeter Funnel, ASTM International, West Conshohocken, 2013.
- [27] C. Weingarten, D. Buchbinder, N. Pirch, W. Meiners, K. Wissenbach, R. Poprawe, Formation and reduction of hydrogen porosity during selective laser melting of AlSi10Mg, *J. Mater. Process. Technol.* 221 (0) (2015) 112–120.
- [28] D. Dai, D. Gu, Thermal behavior and densification mechanism during selective laser melting of copper matrix composites: simulation and experiments, *Mater. Des.* 55 (0) (2014) 482–491.
- [29] N.T. Aboulkhair, N.M. Everitt, I. Ashcroft, C. Tuck, Reducing porosity in AlSi10Mg parts processed by selective laser melting, *Additive Manufacturing* (2014) 77–86 1–4(0).
- [30] ASTM, E2546-07 Standard Practice for Instrumented Indentation Testing, ASTM International, West Conshohocken, 2007.
- [31] I. Yadroitsev, P. Bertrand, I. Smurov, Parametric analysis of the selective laser melting process, *Appl. Surf. Sci.* 253 (19) (2007) 8064–8069.
- [32] I. Yadroitsev, A. Gusarov, I. Yadroitsava, I. Smurov, Single track formation in selective laser melting of metal powders, *J. Mater. Process. Technol.* 210 (12) (2010) 1624–1631.
- [33] S. Yang, J.R.G. Evans, Metering and dispensing of powder; the quest for new solid free forming techniques, *Powder Technol.* 178 (1) (2007) 56–72.
- [34] R. Li, Y. Shi, Z. Wang, L. Wang, J. Liu, W. Jiang, Densification behavior of gas and water atomized 316L stainless steel powder during selective laser melting, *Appl. Surf. Sci.* 256 (13) (2010) 4350–4356.
- [35] N.T. Aboulkhair, I. Maskery, I. Ashcroft, C. Tuck, N.M. Everitt, The Role of Powder Properties on the Processability of Aluminium Alloys in Selective Laser Melting, *Lasers in Manufacturing*, Munich, Germany, 2015.
- [36] E.O. Olakanmi, Selective laser sintering/melting (SLS/SLM) of pure Al, Al-Mg, and Al-Si powders: effect of processing conditions and powder properties, *J. Mater. Process. Technol.* 213 (8) (2013) 1387–1405.
- [37] C. Suryanarayana, Mechanical alloying and milling, *Prog. Mater. Sci.* 46 (1–2) (2001) 1–184.
- [38] W. Zhou, S. Bang, H. Kurita, T. Miyazaki, Y. Fan, A. Kawasaki, Interface and interfacial reactions in multi-walled carbon nanotube-reinforced aluminum matrix composites, *Carbon* 96 (2016) 919–928.
- [39] A.M.K. Esawi, K. Morsi, A. Sayed, A.A. Gawad, P. Borah, Fabrication and properties of dispersed carbon nanotube-aluminum composites, *Mater. Sci. Eng. A* 508 (1) (2009) 167–173.
- [40] S.R.B. Arvind Agarwal, Debrupa Lahiri, *Carbon Nanotubes: Reinforced Metal Matrix Composites*, first ed., CRC Press, 2017.
- [41] T. Etter, P. Schulz, M. Weber, J. Metz, M. Wimpler, J.F. Löffler, P.J. Uggowitzer, Aluminium carbide formation in interpenetrating graphite/aluminium composites, *Mater. Sci. Eng. A* 448 (1) (2007) 1–6.
- [42] L. Ci, Z. Ryu, N.Y. Jin-Phillipp, M. Rühle, Investigation of the interfacial reaction between multi-walled carbon nanotubes and aluminum, *Acta Mater.* 54 (20) (2006) 5367–5375.
- [43] B. Novak, K. Tschöpe, A.P. Ratvik, G.T., Fundamentals of aluminium carbide formation, in: S. C.E (Ed.), *Light Metals 2012*, Springer, Cham, 2012.
- [44] A. Urena, J.M. Gomez De Salazar, L. Gil, M.D. Escalera, J.L. Baldonedo, Scanning and transmission electron microscopy study of the microstructural changes occurring in aluminium matrix composites reinforced with SiC particles during casting and welding: interface reactions, *J. Microsc.* 196 (1999) 124–136 (# (Pt 2)).
- [45] X. Wang, S. Kustov, J. Van Humbeeck, A short review on the microstructure, transformation behavior and functional properties of NiTi shape memory alloys fabricated by selective laser melting, *Materials* 11 (9) (2018).
- [46] J. Ma, B. Franco, G. Tapia, K. Karayagiz, L. Johnson, J. Liu, R. Arroyave, I. Karaman, A. Elwany, Spatial control of functional response in 4D-Printed active metallic structures, *Sci. Rep.* 7 (2017) 46707.
- [47] M.S. Dresselhaus, A. Jorio, M. Hofmann, G. Dresselhaus, R. Saito, Perspectives on carbon nanotubes and Graphene Raman spectroscopy, *Nano Lett.* 10 (3) (2010) 751–758.
- [48] D.D. Phuong, P.V. Trinh, N.V. An, N.V. Luan, P.N. Minh, R.K. Khisamov, K.S. Nazarov, L.R. Zubairov, R.R. Mulyukov, A.A. Nazarov, Effects of carbon nanotube content and annealing temperature on the hardness of CNT reinforced aluminum nanocomposites processed by the high pressure torsion technique, *J. Alloy. Comp.* 613 (2014) 68–73.
- [49] J. Jia, D. Liu, S. Zhang, B. Zhang, S. Liu, G. Ji, Effects of CNTs content on microstructure and mechanical properties of Cnt/ $\alpha$ -Al<sub>2</sub>O<sub>3</sub> and Cnt-Csf/ $\alpha$ -Al<sub>2</sub>O<sub>3</sub> composites, *Ceram. Int.* (2019), <https://doi.org/10.1016/j.ceramint.2019.06.253> in press.
- [50] L.A. Batista, M.D.V. Felisberto, L.S. Silva, T.H.R. da Cunha, E.M. Mazzer, Influence of multi-walled carbon nanotubes reinforcements on hardness and abrasion behaviour of porous Al-matrix composite processed by cold pressing and sintering, *J. Alloy. Comp.* 791 (2019) 96–99.
- [51] E.I. Salama, A. Abbas, A.M.K. Esawi, Preparation and properties of dual-matrix carbon nanotube-reinforced aluminum composites, *Compos. Appl. Sci. Manuf.* 99 (2017) 84–93.
- [52] F. Ostovan, K.A. Matori, M. Toozandehjani, A. Oskoueian, H.M. Yusoff, R. Yunus, A.H. Mohamed Ariff, Nanomechanical behavior of multi-walled carbon nanotubes particulate reinforced aluminum nanocomposites prepared by ball milling, *Materials* 9 (3) (2016) 140.
- [53] P.V. Trinh, N.V. Luan, D.D. Phuong, P.N. Minh, A. Weibel, D. Mesguich, C. Laurent, Microstructure, microhardness and thermal expansion of CNT/Al composites prepared by flake powder metallurgy, *Composites Part A, Applied Science and Manufacturing* 105 (2018) 126–137.
- [54] J.Z. Liao, J.J. Pang, M.J. Tan, Nanoindentation of multi-wall CNT reinforced Al composites, *Advanced Precision Engineering* 447–448 (2010) 549–553.
- [55] M. C.B. R. Shadakhari, Aluminium reinforced metal matrix composites for multi-wall carbon nanotubes -a review, *International Journal of Innovative Research in Science, Engineering and Technology* 6 (5) (2017).